Matrix Stiffness Induces Midnolin-dependent Lamin B1 Degradation to Control Myoblast Differentiation

Liping Guo[1,2,3,9], Yanjing Zhao[1,4,9], Zhe Zhang[1], Chang Sun[1,5], Yafan Xie[6], Qin Dai[1,7,8], Yan Yan[4], Yaoqi Zhou[1], Yang Zhang[1], Quhuan Li[2,*], Juhui Qiu[6,*], Qin Peng[1,*]

[1] Institute of Systems and Physical Biology, Shenzhen Bay Laboratory, Shenzhen, China.

[2] School of Biology and Biological Engineering, South China University of Technology, Guangzhou, China.

[3] School of Life Science and Technology, Harbin Institute of Technology, Harbin, China.

[4] Division of Life Science, Hong Kong University of Science and Technology, Clear Water Bay, Kowloon, Hong Kong, China.

[5] Department of Pathology and Experimental Therapeutics, Faculty of Medicine and Health Sciences, Barcelona University, Barcelona, Spain.

[6] Key Laboratory for Biorheological Science and Technology of Ministry of Education, State and Local Joint Engineering Laboratory for Vascular Implants, College of Bioengineering, Chongqing University, Chongqing, China.

[7] Shenzhen Medical Academy of Research and Translation (SMART), Shenzhen, Guangdong, China

[8] Westlake University, Hangzhou, China

[9] These authors contributed equally.

*Correspondence: pengqin@szbl.ac.cn (Q.P.) , jhqiu@cqu.edu.cn (J.Q.), liqh@scut.edu.cn (Q.L.)

Abstract

Cells decode mechanical cues to direct fate decisions through nuclear remodeling, yet nuclear adaptors to mechanical signals remain elusive. Here, we show that soft matrix suppresses myoblast differentiation and induces nuclear abnormality within 30 minutes, accompanied by a greater than 60% reduction in lamin B1 proteins levels. Mechanistically, midnolin interacts with lamin B1 and mediates ubiquitination-independent degradation of lamin B1 on soft matrix, through the Catch domain of midnolin engaging a β-strand within lamin B1's Ig-like domain. Functionally, moderate lamin B1 expression is essential for myoblast differentiation initiation, as its depletion either by siRNA or CRISPR knockout abolishes myogenic capacity. Our findings reveal that the midnolin-proteasome axis directly converts mechanical inputs into lineage commitment by triggering lamin B1 degradation, defining a novel nuclear mechano-adaptation pathway.

Keywords: Matrix stiffness; Lamin B1 degradation; midnolin-proteasome pathway; myoblast differentiation

Introduction

Mechanical stimuli in the cellular microenvironment are powerful regulators of cell function and behavior, such as extracellular matrix (ECM) elasticity and mechanical strain can significantly influence the fate decision of stem and progenitor cells (Baghdadi *et al*, 2024; Shiraishi *et al*, 2023). The basic mechanism is that stem cells sense mechanical cues and then active downstream signaling events and ultimately results in cell fate transitions and even participates in diseases development (Fiore *et al*, 2025). For example, studies in satellite cells or the differentiation of muscle progenitor cells (Kjaer, 2004; Thomas *et al*, 2015; Zhang *et al*, 2021) revealed that the structural remodeling and stiffness of the ECM are involved in Duchenne muscular dystrophy (Long *et al*, 2024), both reduced mechanical loading and low ECM stiffness suppress cell differentiation and muscle regeneration, causing muscle disuse atrophy (Gibbons *et al*, 2018; Kjaer, 2004; Wall *et al*, 2013). Hence, the cellular and molecular mechanistic understanding of how cells sense mechanical cues are still the potential mechanical determinators of cell fate.

The nucleus, as the stiffest cellular organelle, perceives mechanical cues through cytoskeletal connections and the linker of nucleoskeleton and cytoskeleton (LINC) complex-mediated mechanotransduction (De Belly *et al*, 2022; Dupont & Wickstrom, 2022; Kalukula *et al*, 2022; Maurer & Lammerding, 2019; Nava *et al*, 2020). This mechanosensing capability enables dynamic modulation of nuclear morphology and transcriptional programs, ultimately influencing cell fate decisions. On stiff matrices, nuclei typically adopt a flattened and elongated morphology, which is associated with differentiated cell states. In contrast, on soft matrices, nuclei remain more rounded, exhibiting nuclear envelope (NE) wrinkling and reduced volume-a configuration that helps maintain stem cell pluripotency (Cosgrove *et al*, 2021; Lovett *et al*, 2013; Nguyen *et al*, 2024; Price *et al*, 2017; Virdi & Pethe, 2022). The proper adaptation from the nucleus to the extracellular mechanics is typically called nuclear mechano-adaptation, which requires the nuclear skeleton to rapidly adapt the changes to maintain nuclear integrity (Echarri *et al*, 2019). However, there are lacking a precise explanation of the temporal and molecular basis underpinning nuclear adaptation to the mechano-microenvironment (Beedle & Roca-Cusachs, 2023).

NE proteins maintain the structural integrity and stability of the nuclei. Loss of nuclear skeleton lamina proteins can cause nuclear envelope wrinkling and alterations in nuclear volume (Vahabikashi *et al*, 2022). Previous studies showed that loss of lamin A tends to increase nuclear volume while loss of lamin B1 behaves in the opposite way (Swift *et al*, 2013; Vahabikashi *et al.*, 2022). Lamin B1 expression is responsible for nuclear elasticity to stabilize chromatin condensation (Wintner *et al*, 2020). However, the timescales and mechanism on how lamin B1 loss adapts to the mechano-microenvironment is not well understood. Currently, there

are three pathways related to protein loss or degradation, which are ubiquitination-dependent proteasome pathway (Pohl & Dikic, 2019), midnolin-proteasome pathway for ubiquitination-independent degradation (Gu *et al*, 2023), as well as autophagy-lyososomal pathway (Pohl & Dikic, 2019). It is reported that lamin B1 undergoes degradation through ubiquitination-regulated pathways by E3 ligases (Khanna *et al*, 2018; Krishnamoorthy *et al*, 2018), or autophagic degradation after oncogenic damage (Dou *et al*, 2015). The mechanism underlying ECM stiffness-dependent regulation of lamin B1 proteostasis remains unclear.

In this study, we observed the significant reduction of myoblast differentiation on soft matrices, which was attributed to time-dependent nuclear abnormalities. We analyzed that the major change of nuclear membrane proteins was lamin B1 reduction on soft matrix. To elucidate the underlying mechanism, we investigated different pathways that regulate proteostasis and identified that midnolin mediated lamin B1 degradation via a β-strand capture mechanism in the ubiquitination-independent proteasome pathway on soft matrix. Furthermore, we explored the consequences of lamin B1 reduction in myoblast differentiation. We found that lamin B1 upregulation is required in the early stages of differentiation and influences key myoblast differentiation regulators: *Myod1* and *Wnt4*. Our findings suggest that lamin B1 serves as a critical regulator of nuclear mechanoadaptation and is indispensable for proper myoblast differentiation.

Results

Soft Matrix attenuates myoblast differentiation related to nuclear abnormalities

To explore the effect of mechanical cues on muscle cell differentiation, mouse myoblasts were cultured on polyacrylamide (PAA) hydrogels with stiffnesses of 0.2 kPa (soft), mimicking atrophic muscle conditions, and 10 kPa (stiff), resembling healthy muscle stiffness (Fig. 1A and EV1A). RNA sequencing (RNA-seq) categorized the biological process of differentially expressed genes (DEGs) by Gene Ontology (GO) analysis, revealing significant alternations in cell fate and differentiation catalogers under soft matrix condition (Fig. 1B).

We further induced primary myoblast differentiation with 2% horse serum on different stiffness matrix. Our results demonstrated that myoblast fusion, as indicated by myosin heavy chain 4 (MYH4) expression, was markedly suppressed on soft matrix relative to stiff matrix following 7 days of differentiation induction (Fig. 1C-E). Similar results were from myoblast cell line C2C12 after 7 days induction (Fig. 1F-H), and this inhibition was evident as early as day 3 (Fig. EV1B, C).

RNA-seq also indicated the enrichment of the pathway related to DNA repair (Fig. 1B), suggesting that the impaired myoblast differentiation might be associated with the accumulation of DNA damage. To test this hypothesis, we checked DNA damage dynamics in cells cultured on matrix of varying stiffness during the initial 72-hour differentiation period. More

phosphorylated H2AX at Ser139 (γH2AX)-positive nuclei were detected on soft matrix (Fig. 1I-K), demonstrating that soft matrix caused more DNA damage and may subsequently affected myoblast differentiation. Furthermore, nuclear abnormalities formed prior to a bulk accumulation of γH2AX. Immunostaining revealed a significant alteration of nuclear morphology in 1 Day (Fig. 1M). In particular, 16.7% C2C12 cells cultured on soft matrix displayed a marked increase in nuclear blebbing and micronuclei (MN) formation (Fig. 1L).

In addition, immunostaining results showed that soft matrix hindered F-actin assembly in the early stage of cell adhesion (0.5 hours) followed by gradual spreading (3 hours) in C2C12 (Fig. 1N, O). Nucleus, as a mechanosensor, responds to external forces transmitted from the cytoskeleton and deforms accordingly (Kalukula *et al.*, 2022). Our results showed a significant reduction in nuclear volume on soft matrix, compared to stiff matrix (Fig. 1P).

Taken together, myoblast differentiation is inhibited when myoblasts cultured on soft matrix. Our findings indicate that this inhibition involves a time-dependent cellular adaptation process. Initially, within several minutes, cells on soft matrix exhibited reduced spreading capacity and nuclear volume. Subsequently, within several hours, nuclear morphological abnormalities emerged, subsequently triggering γH2AX foci formation as a marker of DNA damage response. These sequential events collectively contribute to the suppression of myoblast differentiation over extended culture periods (Fig. 1Q).

Lamin B1 Decreases with Reduced Nuclear Volume on Soft Matrix

Nucleus abnormalities are influenced by NE proteins such as lamin A/C and lamin B1, which serve as nuclear skeleton with mechanical properties (Vahabikashi *et al.*, 2022). Therefore, we were curious about how nuclear envelop proteins are responsible for maintaining nucleus morphology and volume on matrix. Here we screened the level changes of the majority of NE proteins that have been reported to be associated with mechano-signaling pathways (Donnaloja *et al*, 2019; Kalukula *et al.*, 2022) by western blot, including Nucleoporin 153 (NUP153), SUN1/2, lamin B receptor (LBR), emerin, lamina associated protein 2β (LAP2β), lamin A/C, lamin B1 (Fig. 2A). Our western blot results showed that the protein levels of lamin A/C was lower on soft matrix as previously reported (Swift *et al.*, 2013), meanwhile both lamin B1 and LAP2β decreased significantly on soft matrix (Fig. 2B and Fig. EV2A, B). Based on the quantitative analysis, reduction of lamin B1 protein level on soft matrix was the most among all the NE proteins at 0.5 hours post cell seeding (Fig. 2B, C). Additionally, lamin B1, which is critical for myoblast differentiation, represents a novel mechanism in nuclear mechano-adaptation. Therefore, we selected lamin B1 as a biomarker to investigate nuclear mechanosensing dysregulation in muscle atrophy. Immunostaining further confirmed that lamin B1 protein level reduced on soft matrix (Fig. 2D, E). This reduction was similarly observed in

primary myoblasts (Fig. 2F, G), confirming the stiffness-dependent regulation of lamin B1. Next, we detected lamin B1 protein levels over a day and found that the low lamin B1 level on soft matrix was retained over the time from 0.5 hours to 24 hours (Fig. 2H, I). Consistent reduction of lamin B1 protein levels on soft matrix was observed in both whole-cell lysates and nuclear fractions (Fig. EV2C-E). Altogether, these results implicate that matrix stiffness modulates the physical deformation of nucleus via modulation of lamin B1 protein level.

Lamin B1 is Degraded by Proteosome Pathway on Soft Matrix

Cells maintain proteostasis by dynamically balancing protein synthesis and degradation in response to external stimuli. To elucidate the mechanism underlying the differential lamin B1 expression observed between 0.2 kPa and 10kPa matrix, we investigated whether this regulation was mediated through changes in protein synthesis or altered degradation kinetics (Fig. 3A).

To investigate the influence of matrix stiffness on lamin B1 protein synthesis, firstly we performed RNA sequencing analysis of C2C12 myoblasts cultured on matrix of varying stiffness at two critical timepoints (0.5 hours and 12 hours) post-seeding. RNA-seq analysis demonstrated comparable mRNA expression levels of *Lmnb1* between soft and stiff matrix at 0.5 hours. However, by 12 hours, stiff matrix exhibited significantly elevated *Lmnb1* transcript levels. These findings indicate that the rapid decline in lamin B1 protein observed on soft matrix (Fig. 2B) is mediated through post-transcriptional regulation rather than reduced gene expression (Fig. 3B, C). Secondly, to determine whether translation was mediated by matrix stiffness, we confirmed by puromycin incorporation that global protein synthesis is unaffected by matrix stiffness (Fig. 3D, E), suggesting that matrix stiffness does not affect protein translation in adhesion process.

C2C12 myoblasts were then plated onto soft or stiff matrices in the presence or absence of cycloheximide (CHX), a selective inhibitor of translational elongation (Fig. 3A). CHX was added to the cell suspension before seeding. Our results showed that, lamin B1 protein level decreased significantly on soft matrix after 0.5 hours of CHX treatment compared to DMSO group (Fig. 3F, G), whereas no change was observed on stiff matrix. To measure the kinetics of lamin B1 protein degradation when cells were exposed to soft and stiff matrix, we treated C2C12 cells with CHX at different time points to assess the stability of lamin B1. Our results showed that B1 exhibited degradation kinetics on 0.2 kPa matrix, with significant protein loss detectable within 30 minutes of treatment. In contrast, lamin B1 remained stable for at least 60 minutes on 10 kPa matrix (Fig. 3H, I), demonstrating stiffness-dependent regulation of lamin B1 proteostasis.

Collectively, our findings demonstrate that accelerated protein degradation serves as the primary mechanism underlying the depletion of lamin B1 on soft matrix. Protein degradation

occurs primarily through two evolutionarily conserved pathways: the ubiquitin-proteasome system and autophagy-lysosome pathway, which collectively mediate the controlled breakdown of proteins into reusable amino acids and short peptides (Fig. 3J) (Balchin *et al*, 2016; Pohl & Dikic, 2019). Inhibition of proteasomal degradation using MG132 attenuated the decrease in lamin B1 protein level on soft matrix, while there was no effect on the cells on stiff matrix (Fig. 3K, L). A similar trend was observed upon treatment with bafilomycin A1 (Baf A1), which blocks autophagosome–lysosome fusion (Fig EV3A, B), suggesting that multiple degradation pathways may be involved under soft matrix. To examine potential autophagic degradation, we monitored LC3 lipidation, a marker of autophagy pathway activation (Fig. 3J). Quantitative analysis revealed no significant difference in the LC3-II/LC3-I ratio between soft and stiff matrix (Fig. 3M-O). Immunofluorescence results further confirmed lamin B1 protein level and nuclear volume was significantly recovered with MG132 treatment but not Baf A1 (Fig. 3P-R). These results demonstrate the proteasome-dominant degradation of lamin B1 protein is regulated by matrix stiffness.

Midnolin-proteasome pathway mediates lamin B1 degradation on soft matrix

Given that conventional protein degradation pathways rely on ubiquitination (Pohl & Dikic, 2019), we sought to investigate the mechanoadaptation mechanism underlying lamin B1 degradation on soft matrix. First, we treated C2C12 cells with MG132 and conducted co-immunoprecipitation (Co-IP) analysis. No substantial ubiquitination on lamin B1 protein was detected on soft matrix (Fig. EV4A), implying lamin B1 degradation occurs through ubiquitination-independent proteasomal pathway.

Latest study identified a novel ubiquitin-independent proteasomal degradation pathway mediated by the nuclear protein midnolin (Gu *et al.*, 2023). Midnolin captures proteins through its Catch domain and guides them to proteasomal degradation (Fig. 4A). To determine whether midnolin contributes to lamin B1 degradation, we firstly checked midnolin levels on different stiffness matrix. Our results revealed a significant decrease in midnolin protein levels in C2C12 cells cultured on 0.2 kPa matrix compare to 10 kPa matrix within 30 minutes of seeding. This autoregulatory reduction in midnolin abundance on soft matrix mirrors the mechanosensitive degradation kinetics observed for lamin B1 (Fig. 4B, C). Midnolin knockdown by siRNA significantly elevated lamin B1 levels on soft matrix but no significant effect on stiff matrix, demonstrating that midnolin-mediated lamin B1 degradation is stiffness-dependent (Fig. 4D, E and Fig. EV4B). Immunofluorescence results further confirmed a two-fold increase in lamin B1 levels on soft matrix upon midnolin knockdown compared to the control group (Fig. 4F, G). However, midnolin knockdown did not prevent nuclear volume reduction (Fig. 4F, H), implying other mechano-sensitive nuclear morphology involves midnolin-independent pathways, potentially mediated by other NE components.

To further investigated the potential interaction between midnolin and lamin B1, we transiently transfected GFP-midnolin into human embryonic kidney (HEK)-293T cells, and seeded them onto

different stiffness matrix. Consistent with observations in C2C12 cells, lamin B1 levels significantly reduced on soft matrix in HEK293T cells (Fig. EV4C, D), suggesting conservation of this mechanoadaptive response across cell types. To study their direct binding, we treated GFP-midnolin overexpressed HEK293T cells with MG132 to stabilize potential transient interactions. Co-IP and immunoblotting assays confirmed that midnolin did interact with lamin B1 specifically on 0.2 kPa matrix but not on 10 kPa matrix (Fig. 4I, J). Additionally, in situ proximity ligation assay (PLA) revealed the specific interaction between lamin B1 and midnolin in HEK293T cells expressing GFP-midnolin on matrix, with higher PLA signals on 0.2 kPa, and the binding specificity was validated by *LMNB1* knockdown (Fig. 4K, L and Fig. EV4E-H). Therefore, both Co-IP and PLA provided the direct evidence for the interaction between midnolin and lamin B1 in those cells on 0.2 kPa matrix. Moreover, super-resolution imaging analysis further showed that the colocalization of midnolin and lamin B1 increased in C2C12 cells after MG132 treatment for 0.5 hours on soft matrix but not on stiff matrix (Fig. EV4I, J).

To elucidate the structural basis of midnolin-lamin B1 interaction, we predict their binding interface through AlphaFold. Notably, the simulation revealed that midnolin's Catch domain specifically recognizes and engages a β-strand within the Ig-like domain of lamin B1, forming a five-stranded antiparallel β-sheet tertiary structure (Fig. 4M). This structural interface precisely matches the reported β-strand capture mechanism of midnolin-mediated proteasomal targeting (Gu *et al.*, 2023). We next performed Co-IP experiments to identify β-stand of lamin B1 that are required for its interaction with midnolin. Deletion of the β-stand of lamin B1 disrupted the stable association of lamin B1 with midnolin on soft matrix (Fig. 4N-P). Notably, deletion of the C-terminal CAAX motif, a membrane-anchoring domain, did not affect lamin B1 binding to midnolin, indicating that this domain is dispensable for their stable interaction (Fig. EV4K-M). Together, these data demonstrate that the degradation of lamin B1 on soft matrix is dependent on midnolin mediated proteasomal degradation pathway.

Loss of lamin B1 attenuates myoblast differentiation

To investigate the functional consequences of midnolin-mediated stiffness-dependent lamin B1 degradation, we first asked whether preventing lamin B1 degradation could rescue muscle atrophy on soft matrix. Knockdown of midnolin in C2C12 cells restored expression of lamin B1 and rescued myoblast differentiation on soft matrix (Fig. 5A-D). To validate the specific effect of midnolin on lamin B1 in myoblast differentiation, we reconstituted *Lmnb1*-null C2C12 cells with either wild-type (WT) lamin B1 or a mutant lacking the midnolin-binding β-strand, and then differentiated them on soft matrix. Our results showed that, the mutant group exhibited significantly higher lamin B1 protein levels on soft matrix, compared to WT group, proving that it can prevent lamin B1 from midnolin-mediated degradation (Fig. 5E-G). Most importantly, the expression of the midnolin-binding-deficient lamin B1 mutant significantly restored myoblast differentiation on soft matrix, whereas WT lamin B1 failed to do so (Fig. 5H-J), demonstrating the specific role of lamin B1

degradation in the stiffness-dependent differentiation.

We then examined the potential role of lamin B1 in myoblast differentiation. We directly used siRNA and CRISPR/Cas9 systems to verify the function of lamin B1 in myotube formation. Knockdown of *Lmnb1* reduced myoblast differentiation a lot, while knockout of *Lmnb1* completely abolished myoblast differentiation (Fig. 5K-M). This suggested that lamin B1 is required for myoblast differentiation. Subsequently, we demonstrated lamin B1 protein level indeed dynamically changed during C2C12 differentiation with a significant increase observed within the critical early stage (< 3 hours post-induction), implying its potential role for initiating myoblast differentiation (Fig. 5N, O). To determine its functional effect, GO analysis of upregulated genes identified non-canonical Wnt signaling as an affected pathway during this early stage (Fig. 5P). Further analysis implicated the involvement of *Wnt4*, a known regulator of skeletal muscle development (Takata *et al*, 2007; Tanaka *et al*, 2011), as a key component of these regulatory networks (Fig. 5Q). Consistent with these findings, *Lmnb1* knockdown resulted in significantly reduced *Wnt4* expression during differentiation, with the most pronounced decrease occurring at 6 hours post-induction (Fig. 5R and Fig. EV5A). We next examined key myogenic regulator: *Myod1*, which drives differentiation (Olguín & Pisconti, 2012). qPCR analysis showed that *Lmnb1* knockdown caused sustained dysregulation of *Myod1* expression patterns throughout myoblast differentiation (Fig. 5S). Collectively, these results suggested that the decrease of lamin B1 protein attenuates myoblast differentiation through downregulating differentiation-related genes in myoblasts specifically. We next examined whether lamin B1 depletion affects genomic stability during differentiation. Strikingly, *Lmnb1*-deficient C2C12 cells exhibited a significant increase in γH2AX foci (Fig. 5T-V). These findings suggest that lamin B1 maintains genomic integrity during myogenesis, and its loss leads to both DNA damage accumulation and impaired differentiation.

We further generated C2C12 cells stably overexpressing lamin B1, constitutive lamin B1 expression impaired rather than enhanced myoblast differentiation (Fig. EV5B). Time-course analysis revealed that endogenous lamin B1 protein levels progressively declined during prolonged differentiation (Fig. EV5C, D), suggesting its functional requirement is restricted to early differentiation stages. Taking together, these results demonstrate that lamin B1 mediates stiffness-dependent regulation of myoblast differentiation, where its transient early expression is required for differentiation initiation.

Discussion

Collectively, our data discover that low matrix stiffness induces disruption of nuclear integrity in hindering myoblast differentiation. To elucidate the nuclear skeleton in regulation of nuclear integrity under mechanical stimulation, we observed lamina protein reduction in C2C12 exposed to soft matrix. Notably, we revealed that the transient lamin B1 protein decrease relays on ubiquitination-independent midnolin-proteasome degradation pathway via a β-strand

capture mechanism. In addition, the soft matrix-induced lamin B1 degradation impedes myoblast differentiation into myotubes, potentially mediated by reduced expression of *Wnt4* and *Myod1* following lamin B1 knockdown. These results suggest that soft matrix enhances midnolin-lamin B1 interaction to promote lamin B1 proteasomal degradation, leading to nuclear abnormalities, DNA damage, and subsequent repression of *Wnt4* and *Myod1* expression, ultimately impairing myoblast differentiation (Fig. 5W). These data uncover a previously unrecognized relationship whereby matrix stiffness modulates lamin B1 protein levels to govern myoblast differentiation.

Nuclear mechanics has emerged as a central focus in cellular mechanobiology research. Our findings demonstrate that ECM stiffness modulates nuclear lamina organization and transcriptional programs to drive cell fate decisions (Fig. 1), which is consistent with previous reports (De Belly *et al.*, 2022; Nava *et al.*, 2020). People have highlighted the ability of lamin A/C responds to mechanical stimuli at both protein level and spatial location, thereby influences the differentiation of MSCs (Buxboim *et al*, 2014; Ihalainen *et al*, 2015; Swift *et al.*, 2013). In contrast to lamin A/C, lamin B1 - while essential for nuclear membrane integrity - has been primarily characterized for its developmental functions (Chang *et al*, 2022; Vergnes *et al*, 2004), with its potential role in nuclear mechanoadaptation and cell fate regulation remaining largely unexplored. Our data show that lamin B1 decreases on soft matrix, inducing nuclear volume shrinkage and envelope wrinkling phenotypically (Fig. 1-2), which is similar to the phenotype in lamin B1 knockout cells reported by previous studies (Vahabikashi *et al.*, 2022). However, the trends in lamin B1 abundance and nuclear volume are not strictly proportional. We speculate that this imperfect correlation may be attributable to compensatory contributions from lamin A/C, whose levels and organization are also regulated by ECM stiffness (Fig. 2B). This interpretation is supported by prior studies demonstrating that lamin A/C and lamin B1 differentially contribute to nuclear architecture and mechanics (Kim *et al*, 2017; Matias *et al*, 2022; Vahabikashi *et al.*, 2022). Although how distinct lamin subtypes coordinately regulate nuclear mechanical adaptation to ECM cues remains to be elucidated.

We also found that appropriate lamin B1 protein levels are critical for early myoblast formation (Fig. 5), due to the fact that the process of early myoblast differentiation may require nuclear skeleton remodeling. Previous study showed that both LBR and lamin B2 have a tendency to

be up-regulated in early stage of differentiation followed by gradual decrease (Bakay *et al*, 2006). Another NE protein, Emerin, is required for the perinuclear localization and inhibition of expression of *Myod1*, *Myf5*, and *Pax7* (Demmerle *et al*, 2013). *Myod1*, a master regulator of myogenesis, orchestrates myoblast differentiation and exhibits a two-fold upregulation during this process (Crisp *et al*, 2006). While the regulatory relationship between lamin B1 and myogenic factors *Myod1* and *Wnt4* has remained unexplored, our study establishes for the first time that lamin B1 protein levels directly correlate with the dynamics of *Myod1* and *Wnt4* expression during myoblast differentiation. Reduction of lamin B1 level by soft matrix or direct deficiency of lamin B1 lead to DNA damage in cells during myogenic differentiation (Fig. 1 and 5). As a previous study reported, in a differentiation checkpoint where genome integrity needs to be ensured, DNA damage can impede the process of myogenic differentiation (Puri *et al*, 2002).

The 'half-life' of different proteins in the cell is quite variable (Correa Marrero & Barrio-Hernandez, 2021; Eldeeb *et al*, 2019), and this also depends on the types of the stimuli. The half-life of lamin B1 degradation induced by oncogenic injury is longer than a day via the autophagy pathway (Dou *et al.*, 2015), whereas the ubiquitination-dependent proteasomal degradation pathway mediated by E3 ligases also requires a minimum half-life of 6 hours for lamin B1 (Khanna *et al.*, 2018; Krishnamoorthy *et al.*, 2018). However, our results suggest that in addition to the lamin B1 degradation process described above, the response of lamin B1 to mechanical stimuli is dependent on the ubiquitination-independent proteasome pathway (Fig. 3 and 4). As latest study reported, midnolin facilitates substrate degradation with its self-contained Ubl domain, which is a much faster pathway to achieve efficient and protein degradation (Gu *et al.*, 2023). We validated that the specificity of the interaction between midnolin and lamin B1 through the β strand truncation (Fig. 4N-P and 5E-G). Therefore, midnolin-mediated lamin B1 degradation in response to soft matrix represents a precise molecular mechanism underlying nuclear mechano-adaptation.

In summary, we have identified a novel ubiquitination-independent mechanism whereby midnolin targets lamin B1 for proteasomal degradation in response to mechanical cues, leading to nuclear integrity loss. This pathway plays a critical role in myogenesis by modulating the expression of key myogenic regulators *Myod1* and *Wnt4*. Our results establish the midnolin-

mediated lamin B1 degradation pathway as a potential therapeutic lever for intervening in muscle pathologies characterized by defective nuclear mechanotransduction.

Methods

Cell Culture

C2C12 (ATCC, CRL-1772™) and HEK293T (ATCC, CRL-3216™) Cells were propagated in Dulbecco's modified Eagle's medium (DMEM) (Gibco, C11995500) containing 20% Australia origin fetal bovine serum (AFBS) (Sigma, F8318) and 1% penicillin-streptomycin (Gibco, 15140122). Primary myoblasts were a kind gift of Dr. Yang Zhang, and were cultured in Nutrient Mixture F-12 Ham (Sigma, N6658) with 20% AFBS, 5 ng/mL basic FGF (YEASEN, 91330ES10) and 1% penicillin-streptomycin. Cells differentiated with DMEM containing 2% heat-inactivated horse serum (Gibco, 26050088), and cultured at 37 °C with 5% CO_2. All the cells were tested for mycoplasma (BeyoDirect™ Mycoplasma qPCR Detection Kit, C0303S) upon thawing of frozen stocks.

Western blot

Western blots were implemented following standard procedures. Briefly, cells were seeded and cultured on the plates or PAA gels accordingly in 37℃ incubators. After treatment with inhibitors or gels, cells were lysed using RIPA buffer. Following denaturation, lysates were loaded into 10% TGX Stain-Free polyacrylamide gels (Bio-Rad, 1610183) and transferred onto a 0.45 μm PVDF membrane (Immobilon® - P Membrane, IPVH00010). After blocking with 5% non-fat milk (CST, 9999s), the membranes were incubated with primary antibody overnight at 4℃ and with the horseradish-peroxidase (HRP)-conjugated secondary antibody for 1 hour at room temperature. ECL Western Blotting Substrate (Epizyme, SQ201) was used to detect HRP and the bands were visualized with the ChemiDoc MP imaging system (Bio-Rad). The intensity of the bands was analyzed using ImageJ software.

Nuclear fraction assay

In order to separate the nuclear fraction (containing lamin B1) from the cytoplasmic fraction (containing the interfering proteins e.g., BSA), nuclear and cytoplasmic proteins were isolated. Briefly, the cells were washed with DPBS twice and lysed using NE1 buffer (1M HEPES-KOH pH 7.5, 1M KCl, 2 M spermidine, 10% Triton X-100, and 20% glycerol and protease inhibitor). The nuclear fraction and the cytoplasmic fraction were separated by gradient centrifugation.

Immunofluorescence

0.1 million C2C12 cells were seeded for staining experiments or 0.3 million C2C12 cells were used for myotube differentiation experiments on fibronectin (Corning, 356008) coated PAA gels or dishes. They were then fixed with 4% Paraformaldehyde (Biosharp, BL539A) for 30 mins at room temperature. 0.25% Triton X-100 (Sangon Biotech, A110694) was used to permeabilize the cells for 15 mins and block with 5% BSA/PBST for 1 hour. Different

combinations of the following primary antibodies were then used: mouse anti-Lamin B1 (1:500 Santa Cruz Biotechnology), Rabbit anti-Lamin B1 (1:1000 Abcam), and mouse anti myosin4 (1:100 eBioscience™). Cells were incubated with primary antibodies overnight at 4℃. They were then washed three times with TBST for 10 mins. Then, the gels or dishes were incubated with secondary antibodies at room temperature for 1 hour. They were then stained against Hoechst33342 (CST, 4082) or Alexa Fluor™ 568 phalloidin (ThermoFisher, A12380), and washed again with TBST. The gels were then mounted with VECTASHIELD® Antifade Mounting Medium (Vectorlabs, H-1000).

Preparation of polyacrylamide gels and stiffness measurement

PAA gels were prepared as described previously (Tse & Engler, 2010). Briefly, Different concentrations of acrylamide and bis-acrylamide were mixed in a solution to produce gels of different rigidity. The solution also contained 10% Ammonium persulfate (APS) (Sangon Biotech, A100486), and N, N, N', N'-Tetramethylethylenediamine (TEMED) (Sangon Biotech, A610508). The solution was then placed on top of the glass and covered with a coverslip. After 30 mins, the coverslip was removed with Dulbecco's Phosphate-Buffered Sallines (DPBS). The gels were coated with 20 μg/mL fibronectin overnight at 4℃ and 0.1% gelatin (Amresco, 9764) for 1 hour at 37℃ to promote cell adhesion. For subsequent experiments, only fibronectin was used for PAA gel coating to simplify the procedure. After coating, gels were washed with PBST and then seeded cells on. The Young's modulus was measured for both FN-coated and FN&gelatin-coated PAA gels by atomic force microscopy (AFM). AFM measurements used a cylindrical tip with 1 micron end radius (SAA-SPH-1UM, Bruker AFM Probes), which was then mounted on a NanoWizard ULTRA Speed 2 system (Bruker). The stiffness was calibrated by determining a spring constant of the cantilever from the thermal fluctuations at room temperature, ranging from 0.01~1 N/m. The cantilever was moved towards the stage at a rate of 2 μm/s for indentations. JPK Instruments software analyzed AFM-generated F-D curves and calculated the Young's modulus of PAA gels.

Co-immunoprecipitation (Co-IP) assays

Co-IP was conducted as previously described (Tang *et al*, 2022). Briefly, HEK293T cells were transfected with GFP-midnolin using Lipofectamine 3000 reagent (Invitrogen™, L3000001). After transfection 36 hours, cells were treated with MG132 for 6 hours then seeded onto gels for 3 hours. Cells were then washed twice with ice-cold PBS and lysed with IP lysis buffer (Thermo, 87787) containing 100×protease inhibitor (Roche, 11836170001) for 20 mins on ice. After centrifugation at 4°C, 12,000 rpm for 10 mins, the protein supernatant was incubated separately with antibodies against GFP (Abcam, 290), lamin B1 (Abcam, 16048) and rabbit IgG (CST, 2729) at 4 °C overnight with rotation. The immune complexes were then incubated with Protein A/G Magnetic Beads (Vazyme, PB101) for 1 hour at room temperature with rotation. For exogenous Co-immunoprecipitation (Co-IP), HEK293T cells transfected with

plasmid expressing Flag-lamin B1, the supernatants mixed with Anti-Flag Nanobody-Magarose Beads (AlpaLifeBio, KTSM1361) were rotated for 2 hrs at 4 °C. After placing the tube on a magnet to separate the beads from the solution, the supernatant was removed, and the beads were washed three times with lysis wash buffer. Finally, 2×SDS loading buffer was added to each sample for subsequent western blot analysis.

In vivo ubiquitination assay

C2C12 cells were seeded on gels for 30 mins, and then lysed using the IP lysis buffer containing 100×protease inhibitor (Roche, 11836170001) and 5 mM/L N-ethylmaleimide (MedChemExpress, HY-D0843) to prevent de-ubiquitylation for 30 mins on ice. The cell lysates were immunoprecipitated using the antibodies against lamin B1 (Abcam, 16048) and rabbit IgG, and were then subjected to immunoblotting analysis using antibody against Ub (CST, 3933S).

Proximity ligation assay (PLA)

GFP-midnolin overexpression HEK293T Cells were fixed and permeabilized as described for IF analysis. The assays were carried out using a Duolink PLA kit (Sigma-Aldrich, DUO92002 & DUO92004) following the manufacturer's protocol. Briefly, blocking solution was added for 1 hour at 37°C. Then incubated with primary antibodies overnight at 4°C. Each incubation step was followed by washing 2×5 mins in Duolink® In Situ Wash Buffer. PLA probes (PLUS and MINUS) were added and incubated for 1 hour at 37°C. Ligase solution was then added and incubated for 30 mins at 37°C followed by incubation with amplification solution containing polymerase for 100 mins at 37°C and protected from light. The samples were then mounted with Duolink® In Situ Mounting Medium with DAPI (Sigma-Aldrich, DUO82040).

Super-resolution imaging and data analysis

Cells were fixed and prepared as IF described above, and imaging was conducted using a ZEISS Elyra 7 equipped with a 100×/1.46 NA oil immersion objective. Samples were excited with 488 nm and 561 nm lasers, and structured illumination microscopy (SIM) mode was used for reconstruction. All images were processed with ZEISS ZEN software using consistent parameters, including 3D SIM reconstruction, noise filtering, and alignment, to ensure reproducibility. The Pearson's coefficients were rigorously calculated from $\geqslant 5$ cells per condition using Imaris software, analyzing colocalization specifically within nuclear volumes while applying consistent thresholding and background subtraction parameters.

Cell transfection

Plasmid DNA transfection was performed using Lipofectamine 3000 reagent (Invitrogen, L3000001), whereas siRNA transfection was performed using Lipofectamine RNAiMax (Invitrogen, 13778075). All experiments were performed 48 hours after transfection.

The siRNA oligonucleotides for negative control: 5'-UUCUCCGAACGUGUCACGUTT-3' and 5'-ACGUGACACGUUCGGAGAATT-3', *Lmnb1*: 5'-AGAGUCUAGAGCAUGUUUG-3' and 5'-UUCAAGCGAAUAAACUUCCTT-3', *Midn*: 5'-GGAACAGUCCGUUAUGCAATT-3' and 5'-UUGCAUAACGGACUGUUCCTT-3'. The siRNA oligonucleotides for Human cell line: *LMNB1*: 5′-GCATTAAAGCAGCGTATC-3′ (Chang *et al.*, 2022).

RNA isolation and qPCR

Total RNAs were extracted from cultured C2C12 cells using E.Z.N.A. Total RNA Kit I reagent (Omegabiotek, R6834-01) according to the manufacturer's instructions. Isolated RNAs were reversed-transcribed into cDNA with 5 x PrimeScript RT Master Mix (Takara, RR036A). qPCR (Quantitative real-time-polymerase chain reaction) was performed with Hieff® qPCR SYBR Green Master Mix (Yeasen, 11204ES) by using the specific primer pairs. Gene expression was normalized against *GAPDH*. The qPCR primers for *GAPDH* gene were: Forward 5′-CAGAAGACTGTGGATGGCCC-3′ and Reverse 5′-ATCCACGACGGACACATTGG-3′; *Lmnb1* gene: Forward 5′- AAGGCTCTCTACGAGACCGA-3′ and Reverse 5′-TGATCTGGGCTCCACTGAGA-3′; *Myod1* gene: Forward 5′-TACAGTGGCGACTCAGATGC-3′ and Reverse 5′-GTAGTAGGCGGTGTCGTAGC-3′; *Midn* gene: Forward 5′-GCGTCAACTTGCTCCCAT-3′ and Reverse 5′-AACGCCTCAAAGTACCCAAG-3′. *Wnt4* gene: Forward 5′-AAGAGGAGACGTGCGAGAAAC-3′ and Reverse 5′- GTCCCTTGTGTCACCACCTT-3′. Samples were run on a QuantStudio 3 Real-time PCR System (Applied Biosystems).

CRISPR-mediated lamin B1 gene knockout

To knockout lamin B1 genes, we first inserted *mLmnb1* gRNA into pSpCas9(BB)-2A-GFP (PX458) (addgene#48138). Here we designed primers for two gRNAs (gRNA1: 5' TGCAGGCGCGACAGGCGCGT 3', gRNA2: 5' TCTGGAGCTTGGCGCGCTCG 3') and did cloning by using Golden Gate assembly. Plasmids were verified by Sanger sequencing. Then, 0.4 million C2C12 cells were seeded into 6-well plate the day before transfection. 1.25 μg/mL *Lmnb1*-PX458-gRNA1 and 1.25 μg/mL *Lmnb1*-PX458-gRNA2 were co-transfected into C2C12 with Lipofectamine™ 3000 Reagent. 48 hours post-transfection, cells were subjected to FACS to isolate GFP positive single cell clone into 96-well plates. After incubation for about a month, single clone got expanded and verified by genotyping PCR with lamin B1-specific primers (*mLmnb1*-F: 5' GCCTGTGGTTTGTACCTTCG 3', *mLmnb1*-R: 5' TCATTCTTCGGGCCGTTGG 3') as well as Sanger sequencing.

RNA-sequencing

C2C12 cells were treated and sorted as described above to harvest the total RNAs. The RNA integrity was evaluated using the Agilent 2100 Bioanalyzer. Library preparation and sequencing were performed on the Illumina NovaSeq 6000 platform. The sequencing data（Raw

data）underwent quality control using fastp (v2.0) to remove adapters, trim low-quality reads (score < 20), and discard reads with an N content exceeding 10%. The processed reads were then aligned to the GRCm39 reference genome using HISAT2 software (Kim *et al*, 2015). Expression quantification was performed using the StringTie software(Pertea *et al*, 2015) against gene annotation obtained from *Mus musculus* Ensembl release 104 (Aken *et al*, 2016). Differential expression analysis was conducted using the DESeq2 tool (Love *et al*, 2014). Only genes with a fold change greater than 2 and an adjusted *p*-value less than 0.05 were considered differentially regulated. The bioinformatics resources of the Database for Annotation, Visualization, and Integrated Discovery (DAVID)(Dennis *et al*, 2003) were used for functional annotation enrichment analysis of differentially expressed genes.

Prediction of the interaction between lamin B1 and midnolin by AlphaFold

Residues 390-588 of *Lmnb1* sequence (UniProtKB: P14733) was paired with the MIDN sequence (UniProtKB: Q3TPJ7) as the input for multimer prediction by using AlphaFold (v2.3.2). Default reference databases and max_template_data = 2024-04-05 were used during structure prediction. We ran 10 independent predictions, and selected the top-ranking model based on the iptm+ptm score.

Plasmid cloning

The cDNA sequences of lamin B1 were cloned into the pSIN-FLAG vector. Various truncations (Δβ-strand, residues 390 to 404; ΔCAAX motif, residues 527 to 588) of lamin B1 were generated from the pSIN-FLAG-lamin B1 construct to facilitate direct transfection. The cDNA sequences of midnolin were cloned into the pSIN-GFP vector. All newly created constructs in this study were rigorously verified through DNA sequencing to ensure their accuracy and integrity.

The fragment of full-length Lamin B1 was amplified from cDNA library. And then based on the PCR product of full-length Lamin B1, the DNA fragments of Lamin B1 Δ β-strand mutant was generated by multiple PCRs. And eventually pSIN-DD-mCherry-lamin B1 constructs were generated by Gibson Assembly and verified by Sanger sequencing before transfection or virus packaging.

Construction of the DD-mCherry-Lamin B1 stable cell line

To construct the stable cell line, C2C12 *Lamin B1* KO cells were seeded onto a 24-well plate one day before infection. Cells were infected with lentivirus of pSIN-DD-mCherry-lamin B1 WT or pSIN- DD-mCherry-lamin B1 Mutant as well as 10 μg/ml polybrene next day. After 72 h, cells with appropriate expression level of mCherry were selected using FACS.

Puromycin incorporation assay

Puromycin incorporation assay was performed as described (Zhang *et al*, 2018). C2C12 cells were treated with 91 μM puromycin for 5 minutes after plating onto gels 25 minutes. Whole cell lysates were analyzed by Western Blot using a puromycin antibody (Millipore).

Statistical analysis

All data were obtained from at least three independent experiments unless indicated otherwise. GraphPad Prism 9.0.0 (GraphPad Software) was used for statistical analysis. To calculate Pearson's correlation coefficient, the images were processed by Zeiss Elyra7 SIM (Structured Illumination Microscopy) and then analyzed by Imaris (Microscopy Image Analysis Software) for 3D co-localization. The sample size, statistical significance value and error bar graphs were indicated in figure legends.

Graphics

Graphics created and used in the synopsis, panels A and Q of Fig. 1, panel A of Fig. 2, panels A and J of Fig. 3, panels A and M of Fig. 4 and panel W of Fig. 5 were created with BioRender.com.

Data Availability

The bulk RNA sequencing data produced in this study are available in the NCBI database through accession number GSE323368 (https://www.ncbi.nlm.nih.gov/geo/query/acc.cgi?acc=GSE323368). All other data that support the findings are available as a source data file.

Acknowledgments

This work was financially supported by the National Natural Science Foundation of China (32471370 to Q.P., 12372302 to J.Q., 32271360 to Q.L.), Shenzhen Medical Research Fund (B2402010 to Q. P.), and the Open Sharing Fund for the Large Instruments and Equipments of Shenzhen Bay Laboratory. We thank the Bioimaging Core facility at Shenzhen Bay Laboratory for providing imaging support, specifically thanking engineers Mei Yu and Shixian Huang for assistance with Super-Resolution Microscopes (Zeiss Elyra 7) and Dragonfly Spinning Disk Confocal Microscopy (4-laser), and Engineer Chunyue Zhao for her support with Atomic Force Microscopy. We also acknowledge the usage of BioRender (biorender.com) for creating the figures.

Disclosure and competing interests statement

The authors declare no competing interests.

References

Aken BL, Ayling S, Barrell D, Clarke L, Curwen V, Fairley S, Fernandez Banet J, Billis K, García Girón C, Hourlier T *et al* (2016) The Ensembl gene annotation system. *Database (Oxford)* 2016

Baghdadi MB, Houtekamer RM, Perrin L, Rao-Bhatia A, Whelen M, Decker L, Bergert M, Pérez-Gonzàlez C, Bouras R, Gropplero G *et al* (2024) PIEZO-dependent mechanosensing is essential for intestinal stem cell fate decision and maintenance. *Science* 386: eadj7615

Bakay M, Wang Z, Melcon G, Schiltz L, Xuan J, Zhao P, Sartorelli V, Seo J, Pegoraro E, Angelini C *et al* (2006) Nuclear envelope dystrophies show a transcriptional fingerprint suggesting disruption of Rb-MyoD pathways in muscle regeneration. *Brain* 129: 996-1013

Balchin D, Hayer-Hartl M, Hartl FU (2016) In vivo aspects of protein folding and quality control. *Science* 353: aac4354

Beedle AE, Roca-Cusachs P (2023) The reversibility of cellular mechano-activation. *Curr Opin Cell Biol* 84: 102229

Buxboim A, Swift J, Irianto J, Spinler KR, Dingal PC, Athirasala A, Kao YR, Cho S, Harada T, Shin JW *et al* (2014) Matrix elasticity regulates lamin-A,C phosphorylation and turnover with feedback to actomyosin. *Curr Biol* 24: 1909-1917

Chang L, Li M, Shao S, Li C, Ai S, Xue B, Hou Y, Zhang Y, Li R, Fan X *et al* (2022) Nuclear peripheral chromatin-lamin B1 interaction is required for global integrity of chromatin architecture and dynamics in human cells. *Protein Cell* 13: 258-280

Correa Marrero M, Barrio-Hernandez I (2021) Toward Understanding the Biochemical Determinants of Protein Degradation Rates. *ACS Omega* 6: 5091-5100

Cosgrove BD, Loebel C, Driscoll TP, Tsinman TK, Dai EN, Heo SJ, Dyment NA, Burdick JA, Mauck RL (2021) Nuclear envelope wrinkling predicts mesenchymal progenitor cell mechano-response in 2D and 3D microenvironments. *Biomaterials* 270: 120662

Crisp M, Liu Q, Roux K, Rattner JB, Shanahan C, Burke B, Stahl PD, Hodzic D (2006) Coupling of the nucleus and cytoplasm: role of the LINC complex. *J Cell Biol* 172: 41-53

De Belly H, Paluch EK, Chalut KJ (2022) Interplay between mechanics and signalling in regulating cell fate. *Nat Rev Mol Cell Biol* 23: 465-480

Demmerle J, Koch AJ, Holaska JM (2013) Emerin and histone deacetylase 3 (HDAC3) cooperatively regulate expression and nuclear positions of MyoD, Myf5, and Pax7 genes during myogenesis. *Chromosome Res* 21: 765-779

Dennis G, Sherman BT, Hosack DA, Yang J, Gao W, Lane HC, Lempicki RA (2003) DAVID: Database for Annotation, Visualization, and Integrated Discovery. *Genome Biol* 4: R60

Donnaloja F, Jacchetti E, Soncini M, Raimondi MT (2019) Mechanosensing at the Nuclear Envelope by Nuclear Pore Complex Stretch Activation and Its Effect in Physiology and Pathology. *Front Physiol* 10: 896

Dou Z, Xu C, Donahue G, Shimi T, Pan JA, Zhu J, Ivanov A, Capell BC, Drake AM, Shah PP *et al* (2015) Autophagy mediates degradation of nuclear lamina. *Nature* 527: 105-109

Dupont S, Wickstrom SA (2022) Mechanical regulation of chromatin and transcription. *Nat Rev Genet* 23: 624-643

Echarri A, Pavón DM, Sánchez S, García-García M, Calvo E, Huerta-López C, Velázquez-Carreras D, Viaris de Lesegno C, Ariotti N, Lázaro-Carrillo A *et al* (2019) An Abl-FBP17 mechanosensing system couples local plasma membrane curvature and stress fiber remodeling during mechanoadaptation. *Nat Commun* 10: 5828

Eldeeb MA, Siva-Piragasam R, Ragheb MA, Esmaili M, Salla M, Fahlman RP (2019) A molecular toolbox for studying protein degradation in mammalian cells. *J Neurochem* 151: 520-533

Fiore VF, Almagro J, Fuchs E (2025) Shaping epithelial tissues by stem cell mechanics in development and cancer. *Nat Rev Mol Cell Biol* 26: 442-455

Gibbons MC, Singh A, Engler AJ, Ward SR (2018) The role of mechanobiology in progression of rotator cuff muscle atrophy and degeneration. *J Orthop Res* 36: 546-556

Gu X, Nardone C, Kamitaki N, Mao A, Elledge SJ, Greenberg ME (2023) The midnolin-proteasome pathway catches proteins for ubiquitination-independent degradation. *Science* 381: eadh5021

Ihalainen TO, Aires L, Herzog FA, Schwartlander R, Moeller J, Vogel V (2015) Differential basal-to-apical accessibility of lamin A/C epitopes in the nuclear lamina regulated by changes in cytoskeletal tension. *Nat Mater* 14: 1252-1261

Kalukula Y, Stephens AD, Lammerding J, Gabriele S (2022) Mechanics and functional consequences of nuclear deformations. *Nat Rev Mol Cell Biol* 23: 583-602

Khanna R, Krishnamoorthy V, Parnaik VK (2018) E3 ubiquitin ligase RNF123 targets lamin B1 and lamin-binding proteins. *FEBS J* 285: 2243-2262

Kim D, Langmead B, Salzberg SL (2015) HISAT: a fast spliced aligner with low memory requirements. *Nat Methods* 12: 357-360

Kim JK, Louhghalam A, Lee G, Schafer BW, Wirtz D, Kim DH (2017) Nuclear lamin A/C harnesses the perinuclear apical actin cables to protect nuclear morphology. *Nat Commun* 8: 2123

Kjaer M (2004) Role of extracellular matrix in adaptation of tendon and skeletal muscle to mechanical loading. *Physiol Rev* 84: 649-698

Krishnamoorthy V, Khanna R, Parnaik VK (2018) E3 ubiquitin ligase HECW2 targets PCNA and lamin B1. *Biochim Biophys Acta Mol Cell Res* 1865: 1088-1104

Long AM, Kwon JM, Lee G, Reiser NL, Vaught LA, O'Brien JG, Page PGT, Hadhazy M, Reynolds JC, Crosbie RH *et al* (2024) The extracellular matrix differentially directs myoblast motility and differentiation in distinct forms of muscular dystrophy: Dystrophic matrices alter myoblast motility. *Matrix biology : journal of the International Society for Matrix Biology* 129: 44-58

Love MI, Huber W, Anders S (2014) Moderated estimation of fold change and dispersion for RNA-seq data with DESeq2. *Genome Biol* 15: 550

Lovett DB, Shekhar N, Nickerson JA, Roux KJ, Lele TP (2013) Modulation of Nuclear Shape by Substrate Rigidity. *Cell Mol Bioeng* 6: 230-238

Matias I, Diniz LP, Damico IV, Araujo APB, Neves LDS, Vargas G, Leite REP, Suemoto CK, Nitrini R, Jacob-Filho W *et al* (2022) Loss of lamin-B1 and defective nuclear morphology are hallmarks of astrocyte senescence in vitro and in the aging human hippocampus. *Aging Cell* 21: e13521

Maurer M, Lammerding J (2019) The Driving Force: Nuclear Mechanotransduction in Cellular Function, Fate, and Disease. *Annu Rev Biomed Eng* 21: 443-468

Nava MM, Miroshnikova YA, Biggs LC, Whitefield DB, Metge F, Boucas J, Vihinen H, Jokitalo E, Li X, Garcia Arcos JM *et al* (2020) Heterochromatin-Driven Nuclear Softening Protects the Genome against Mechanical Stress-Induced Damage. *Cell* 181: 800-817 e822

Nguyen J, Wang L, Lei W, Hu Y, Gulati N, Chavez-Madero C, Ahn H, Ginsberg HJ, Krawetz R, Brandt M *et al* (2024) Culture substrate stiffness impacts human myoblast contractility-dependent proliferation and nuclear envelope wrinkling. *J Cell Sci*

Olguín HC, Pisconti A (2012) Marking the tempo for myogenesis: Pax7 and the regulation of muscle stem cell fate decisions. *J Cell Mol Med* 16: 1013-1025

Pertea M, Pertea GM, Antonescu CM, Chang T-C, Mendell JT, Salzberg SL (2015) StringTie enables improved reconstruction of a transcriptome from RNA-seq reads. *Nat Biotechnol* 33: 290-295

Pohl C, Dikic I (2019) Cellular quality control by the ubiquitin-proteasome system and autophagy. *Science* 366: 818-822

Price AJ, Huang EY, Sebastiano V, Dunn AR (2017) A semi-interpenetrating network of polyacrylamide and recombinant basement membrane allows pluripotent cell culture in a soft, ligand-rich microenvironment. *Biomaterials* 121: 179-192

Puri PL, Bhakta K, Wood LD, Costanzo A, Zhu J, Wang JYJ (2002) A myogenic differentiation checkpoint activated by genotoxic stress. *Nat Genet* 32: 585-593

Shiraishi K, Shah PP, Morley MP, Loebel C, Santini GT, Katzen J, Basil MC, Lin SM, Planer JD, Cantu E *et al* (2023) Biophysical forces mediated by respiration maintain lung alveolar epithelial cell fate. *Cell* 186: 1478-1492.e1415

Sun K (2020) Ktrim: an extra-fast and accurate adapter- and quality-trimmer for sequencing data. *Bioinformatics* 36: 3561-3562

Swift J, Ivanovska IL, Buxboim A, Harada T, Dingal PC, Pinter J, Pajerowski JD, Spinler KR, Shin JW, Tewari M *et al* (2013) Nuclear lamin-A scales with tissue stiffness and enhances matrix-directed differentiation. *Science* 341: 1240104

Takata H, Terada K, Oka H, Sunada Y, Moriguchi T, Nohno T (2007) Involvement of Wnt4 signaling during myogenic proliferation and differentiation of skeletal muscle. *Developmental dynamics : an official publication of the American Association of Anatomists* 236: 2800-2807

Tanaka S, Terada K, Nohno T (2011) Canonical Wnt signaling is involved in switching from cell proliferation to myogenic differentiation of mouse myoblast cells. *Journal of molecular signaling* 6: 12

Tang Y, Jia Y, Fan L, Liu H, Zhou Y, Wang M, Liu Y, Zhu J, Pang W, Zhou J (2022) MFN2 Prevents Neointimal Hyperplasia in Vein Grafts via Destabilizing PFK1. *Circ Res* 130: e26-e43

Thomas K, Engler AJ, Meyer GA (2015) Extracellular matrix regulation in the muscle satellite cell niche. *Connect Tissue Res* 56: 1-8

Tse JR, Engler AJ (2010) Preparation of hydrogel substrates with tunable mechanical properties. *Curr Protoc Cell Biol* Chapter 10: Unit 10.16

Vahabikashi A, Sivagurunathan S, Nicdao FAS, Han YL, Park CY, Kittisopikul M, Wong X, Tran JR, Gundersen GG, Reddy KL *et al* (2022) Nuclear lamin isoforms differentially contribute to LINC complex-dependent nucleocytoskeletal coupling and whole-cell mechanics. *Proc Natl Acad Sci U S A* 119: e2121816119

Vergnes L, Péterfy M, Bergo MO, Young SG, Reue K (2004) Lamin B1 is required for mouse development and nuclear integrity. *Proc Natl Acad Sci U S A* 101: 10428-10433

Virdi JK, Pethe P (2022) Soft substrate maintains stemness and pluripotent stem cell-like phenotype of human embryonic stem cells under defined culture conditions. *Cytotechnology* 74: 479-489

Wall BT, Dirks ML, van Loon LJC (2013) Skeletal muscle atrophy during short-term disuse: implications for age-related sarcopenia. *Ageing Res Rev* 12: 898-906

Wintner O, Hirsch-Attas N, Schlossberg M, Brofman F, Friedman R, Kupervaser M, Kitsberg D, Buxboim A (2020) A Unified Linear Viscoelastic Model of the Cell Nucleus Defines the Mechanical Contributions of Lamins and Chromatin. *Adv Sci (Weinh)* 7: 1901222

Zhang K, Daigle JG, Cunningham KM, Coyne AN, Ruan K, Grima JC, Bowen KE, Wadhwa H, Yang P, Rigo F *et al* (2018) Stress Granule Assembly Disrupts Nucleocytoplasmic Transport. *Cell* 173: 958-971.e917

Zhang W, Liu Y, Zhang H (2021) Extracellular matrix: an important regulator of cell functions and skeletal muscle development. *Cell Biosci* 11: 65

Figure legends

Figure 1. Soft matrix impairs myoblast differentiation and increases nuclear abnormalities and DNA damage.
(A) Schematic of hydro-matrices with different stiffness to mimic mechanical loading on cells in healthy and muscular dystrophy conditions (figure created with BioRender.com). **(B)** GO terms analysis of biological processes for upregulated and downregulated genes (0.2 kPa vs. 10 kPa) after 12 hours of culture on matrices. Differential expression was analyzed using the Wald test in DESeq2; $|\log_2 FC| > 1$, adjusted $p < 0.05$). **(C to H)** Representative images of differentiated mouse primary myoblast cells (C) and C2C12 cells (F) on FN-coated PAA matrices after 7 days of 2% horse serum induction. scale bar, 100 µm. **(D, E, G, H)** Quantification data of the fusion index and the percentage of myosin$^+$ cells that ≥ 3 nuclei in (C) and (F), respectively. n = 7 (D and E), 5 (G and H) biological replicates. Statistical significance: (E) $p = 4.10\times10^{-5}$, (G) $p = 2.74\times10^{-7}$, (H) $p = 2.29\times10^{-5}$. **(I to K)** Representative images from C2C12 cells seeded on FN-coated PAA matrices after 3 days of horse serum induction. Hoechst for nuclear staining in blue, γH2AX staining in green and lamin A/C staining in red. Scale bars, 5 µm. **(J, K)** The Quantification of cell numbers with DNA damage (J) and γH2AX foci (K) in (I). n > 40 cells for each condition. $p = 3.92\times10^{-5}$. **(L)** Quantification of cells with nuclear abnormalities in (M). **(M)** Representative images from C2C12 cells seeded on FN-coated PAA matrices after 1 days of horse serum induction. Hoechst for nuclear staining in blue, lamin B1 staining in green and lamin A/C staining in red. White arrows indicate nuclear blebbing and micronuclei formation. Scale bars, 5 µm. n = 3 biological replicates. **(N)** Immunofluorescence of C2C12 cells seeded onto FN and gelatin-coated PAA matrices at 0.5 hours and 3 hours, respectively. Hoechst for nuclear staining in blue and F-actin staining in red. Scale bars, 10 µm. **(O, P)** Fold changes of cell spread area (O) and nuclear volume (P) were quantified from (N). n > 50 cells for each group. Data are presented as the mean ± SD. Tukey's multiple comparisons test. In (O), *p*-values are 2.32×10^{-5}, 1×10^{-10}, and 8.08×10^{-7}, respectively. In (P), *p* -values are 3.88×10^{-8}, 0.1583, and 6.36×10^{-8}, respectively. **(Q)** Summary of hypothesis for soft matrix - mediated inhibition of myoblast differentiation (figure created with BioRender.com). Data information: data in (D, E, G, H, J, K and L) were presented as the mean ± SD. Two-tailed Student's *t*-test was used for statistical analysis.

Figure 2. Soft matrix induces a significant reduction in lamin B1 and maintains this difference over the time consistently.
(A) Schematic diagram of some NE proteins (figure created with BioRender.com). (B, C) Western blot analysis of NE proteins displayed in (A) from C2C12 seeding onto FN and gelatin-coated PAA matrices after 0.5 hours. n = 3 biological replicates, Data are presented as the mean ± SD. Two-tailed Student's *t*-test. (D) Immunofluorescence of C2C12 cells on FN and gelatin-coated PAA matrices. Hoechst for nuclear staining in blue and lamin B1 staining in green. Scale bars, 4 mm. (E) Quantitative analysis of fluorescence intensity of lamin B1 on 0.2 kPa and 10 kPa substrates from (D) (> 300 cells for each group, Two-tailed Student's *t*-test, Data are presented as the mean ± SD). $p = 1\times10^{-10}$. The fluorescence intensity unit is arbitrary unit (AU) and is defined from the detected total fluorescence intensity normalized. (F, G) Western blot analysis of lamin B1 proteins in mouse primary myoblast cells seeded onto FN-coated PAA matrices after 0.5 hours. n = 3 biological replicates. Two-tailed Student's *t*-test, Data are presented as the mean ± SD. (H, I) Western blot analysis of lamin B1 proteins in C2C12 cells seeded onto FN and gelatin-coated PAA matrices at different times. n = 3 biological replicates, Two-way ANOVA/Tukey's multiple comparisons test, Data are presented as the mean ± SD.

Figure 3. Lamin B1 degradation on soft matrix through proteasome pathway.
(A) Schematic diagram of classical protein synthesis pathway. Puromycin is incorporated into nascent polypeptides to detect protein synthesis and assess translation efficiency. Cycloheximide (CHX) inhibits ribosomal activity to block new protein synthesis, enabling tracking of pre-existing protein decay for stability analysis. (Created with BioRender.com). **(B)** Representative genes from RNA-seq were upregulated in pink and downregulated in violet after 0.5 hours and 12 hours culturing on FN and gelatin-

coated PAA matrices (0.2 kPa Vs. 10 kPa). **(C)** The expression of *Lmnb1* from RNA-seq after 0.5 hours and 12 hours culturing on FN and gelatin-coated PAA matrices (0.2 kPa Vs. 10 kPa). n = 3 biological replicates. **(D, E)** C2C12 were treated with 91 μM puromycin for 5 min after seeding onto FN-coated PAA matrices for 25 min and immunoblotted for puromycin. n = 3 biological replicates. **(F, G)** Western blot analysis of lamin B1 protein in C2C12 seeded onto FN and gelatin-coated PAA matrices for 0.5 hours in the presence of protein synthesis inhibitor (CHX, 50 mg/mL). n = 3 biological replicates. **(H, I)** Western blot analysis of lamin B1 proteins stability in C2C12 before seeding (-) and post-seeding onto FN-coated PAA matrices under cycloheximide (CHX) treatment to inhibit protein translation. n = 3 biological replicates. At 0.5 hour, compared to the condition before seeding (t=0), lamin B1 protein level showed a significant decrease on 0.2 kPa gel (***, $p = 0.0001$), while no significant change was observed on 10 kPa gel (ns, no significance, $p = 0.3616$). Data are presented as the mean ± SEM, with two-tailed Student's *t*-test. **(J)** Schematic diagram of two classical protein degradation pathways. Treatment with MG132 inhibits proteasome function by blocking its proteolytic activity, and Baf A1 (bafilomycin A1) inhibits autophagy by inhibiting the fusion between autophagosomes and lysosomes (created with BioRender.com). **(K, L)** Western blot analysis of lamin B1 protein in C2C12 seeded onto FN and gelatin-coated PAA matrices for 0.5 hours in the presence of MG132 (10 μM). n = 3 biological replicates. **(M to O)** Western blot analysis of lamin B1 protein and LC3-II/LC3-I protein in C2C12 seeded onto FN-coated PAA matrices for 0.5 hours in the presence of Baf A1 (100 nM). n = 3 biological replicates. **(P)** Immunofluorescence of C2C12 cells on FN and gelatin-coated 0.2 kPa substrates for 0.5 hours with DMSO or MG132 or Baf A1 treatment. Hoechst for nuclear staining in blue and lamin B1 staining in green. Scale bars, 4 μm. **(Q, R)** Quantitative analysis of the fluorescence intensity of lamin B1 (**Q**) and nuclear volume (**R**) for the images from (**P**) (> 50 cells for each condition, One-way ANOVA/Dunnett's multiple comparisons test. Data are presented as the mean ± SD). In **(Q)**, p -values are 1×10^{-10}, and 0.1285, respectively. In (R), p -values are 1.11×10^{-6} and 0.8826, respectively. Data information: in (C, E, G, L, N, O, Q and R) as the mean ± SD, with Two-tailed Student's *t*-test.

Figure 4. Midnolin-proteasome pathway mediates lamin B1 degradation.

(A) Schematic diagram of midnolin-proteasome pathway: Midnolin contains three main structural domains: the Catch domain, responsible for substrate capture; the C-terminal αHelix-C, binds to the proteasome; and the N-terminal Ubl (ubiquitin-like domain) facilitates substrate degradation. **(B, C)** Representative western blots and quantification analysis show the protein level changes of midnolin in C2C12 seeding onto FN and gelatin-coated PAA matrices for 0.5 hours. n = 3 biological replicates. **(D, E)** Representative western blots and quantification data show the recovery of lamin B1 in response to midnolin knockdown by si-*Midn* in C2C12 after seeding cells on FN-coated PAA matrices for 0.5 hours. n = 5 biological replicates. **(F)** Representative images from negative control scramble siRNA (si-NC) and midnolin knockdown (si-*Midn*) C2C12 cells seeding on 0.2 kPa and 10 kPa FN-coated PAA matrices for 0.5 hours. Scale bars, 10 μm. **(G, H)** Quantification data of lamin B1 intensity (**G**) and nuclear volume (**H**) for fluorescence images in (F) (>50 cells for each condition). In **(G)**, p -values are 0.0347, 1×10^{-10}, and 1.44×10^{-8}, respectively. In (H), p-values are 1×10^{-10}, 0.6907, and 5×10^{-10}, respectively. **(I)** GFP-midnolin HEK293T cells were pre-treated with MG132 for 3 hours and then plated onto FN-coated PAA matrices for 3 hours, Co-IP analysis to detect the interaction midnolin and lamin B1 was performed. IP and IB both with GFP antibody and lamin B1 antibody. **(J)** Normalized Lamin B1/GFP intensity in (**I**). n = 3 biological replicates. Data presented as the mean ± SD. Two-tailed Student's *t*-test was used for statistical analysis. **(K)** In-cell lamin B1 and GFP-midnolin interactions as demonstrated by PLA in the nucleus of HEK293T cells with MG132 treatment on FN-coated PAA matrices. PLA was performed on HEK293T cells transfected with GFP-midnolin. Each red dot indicates the protein-protein interaction between GFP-midnolin and endogenous lamin B1. DAPI was used as the nuclear stain. Scale bar: 10 μm. **(L)** Quantification of PLA signals from experiments as in (K) (Two-tailed Student's *t*-test, Data are presented as the mean ± SD. More than 50 cells for each condition. $p = 1\times10^{-10}$). **(M)** Schematic representation of midnolin and lamin B1. AlphaFold structure prediction of midnolin bound to its substrate lamin B1 (Ig-like domain) reveals an adopted β-strand capture model. **(N)** Schematics of lamin B1 Ig-like domain and β-strand truncation. **(O)** HEK293T cells were transfected with Lamin B1 Ig-like domain or β-strand truncation and cultured on FN-coated 0.2 kPa gels for 3 hours. **(P)** Normalized midnolin/lamin B1 intensity in (O). n = 3 biological replicates. Data information: in (C, E, G, H, J, L and P) were presented as the mean ± SD. Two-tailed Student's *t*-test was used for statistical analysis for (C, E, J, L and P). Tukey's multiple comparisons test was done for (G) and (H).

Figure 5. Lamin B1 protein is essential for myoblast differentiation.

(A) Representative images of si-NC and si-*Midn* C2C12 cells on FN-coated 0.2 kPa gels show the recovery of myoblast differentiation for 3 days. Scale bar, 50 μm. **(B)** Quantitative analysis of fluorescence intensity of lamin B1 from (**A**) (> 100 cells for each group, Two-tailed Student's *t*-test). $p = 4.61\times10^{-9}$. **(C, D)** Quantification data of the fusion index and the percentage of myosin$^+$ cells that ⩾ 3 nuclei in (**A**). n = 5 biological replicates. Two-tailed Student's *t*-test. $p = 1.20\times10^{-5}$. **(E)** Schematics of Inducible lamin B1 WT (full length, FL) and lamin B1 Mutant (β-strand truncation) were established by the fusion of a destabilization domain (DD). Western blot analysis of the protein levels of WT lamin B1 and mutant lamin B1 in *Lmnb1* KO C2C12 cells overexpressing either one of them on 0.2kPa or 10 kPa gels. Cells were pre-treated with 1μM Shield1 for 12 hours before seeding on FN-coated matrices. **(F)** Immunofluorescence of the WT lamin B1 and the mutant lamin B1 in *Lmnb1* KO C2C12 cells overexpressing either one of them with Shield1 pre-treatment (1μM) 12 hours before seeding on FN-coated 0.2 kPa gels. Scale bars, 10 μm. **(G)** Quantitative analysis of fluorescence intensity of lamin B1 from (F) (> 25 cells for each group, Two-tailed Student's t-test). $p = 1\times10^{-10}$. **(H)** Representative images of WT lamin B1 and the mutant in *Lmnb1* KO C2C12 cells on FN-coated 0.2 kPa gels showed the recovery of myoblast differentiation for 3 days. Scale bar, 100 μm. **(I, J)** Quantification data of the fusion index and the percentage of myosin+ cells that ⩾ 3 nuclei in (H) (n = 3. Two-tailed Student's t-test). **(K)** Representative images of WT, si-*Lmnb1*, and *Lmnb1* KO C2C12 cells on petri-dishes with horse serum induced differentiation for 7 days. scale bar, 100 μm. **(L, M)** Quantification data of the fusion index and the percentage of myosin$^+$ cells that ⩾ 3 nuclei in (K). One-way ANOVA/Dunnett's multiple comparisons test. In **(L)**, *p*-values are 1.24×10^{-6} and 1.24×10^{-6}, respectively. **(N, O)** Western blot analysis of lamin B1 dynamics in C2C12 during 2% horse serum induced differentiation on standard petri-dishes, with corresponding intensity quantification data. n = 3 biological replicates. **(P)** GO terms analysis of biological processes for upregulated genes (6 hours Vs. 0 hour) after 2% horse serum induced differentiation. **(Q)** Representative genes from RNA-seq were upregulated in pink and downregulated in violet genes after 2% horse serum induced differentiation. **(R, S)** qPCR to examine the expression of *Wnt4* and *Myod1* during 24 hours differentiation with scramble siRNA (si-NC and si-*Lmnb1*). n = 3 biological replicates. Two-tailed Student's *t*-test. (R) $p = 9.64\times10^{-4}$. (S) $p = 0.0030$. **(T)** Representative images from WT, si-*Lmnb1*, and *Lmnb1* KO C2C12 cells on petri-dishes after 3 days of horse serum induction. Hoechst for nuclear staining in blue, γH2AX staining in green and lamin B1 staining in red. Scale bars, 10 μm. **(U, V)** The Quantification of DNA damage (**U**) and γH2AX foci (**V**) in (**T**). n> 40 cells for each condition. One-way ANOVA/Dunnett's multiple comparisons test. In **(U)**, *p*-values are 1×10^{-10} and 1×10^{-10}, respectively. **(W)** Schematic model representation showing that lamin B1 protein levels are reduced by midnolin mediated proteasomal degradation on soft matrix. Consequently, this leads to reduced transcription of *Wnt4* and *Myod1*, which inhibits the process of myoblast differentiation (figure created with BioRender.com). Data information: data in (B, C, D, G, I, J, L, M, O, R, S, U and V) were presented as the mean ± SD.

Expanded View Figure legends

Figure EV1. Young's modulus of PAA gels and early myoblast differentiation on different matrix.
(A) Young's modulus (*E*, kPa) of PAA hydrogels coated with FN only versus FN combined with Gelatin (n = 3 biological replicates. Data are presented as the mean ± SD). **(B)** Representative images of differentiated C2C12 cells on FN and gelatin-coated PAA matrices after 3 days of 2% horse serum induction. scale bar, 100 μm. **(C)** Quantification data of the fusion index in (B). n = 3 biological replicates, Data are presented as the mean ± SD. Two-tailed Student's *t*-test. $p = 9.96\times10^{-5}$.

Figure EV2. Validation of the molecular weight of SUN2 band and the band shape of Lamin B1.
(A) SUN2 was detected by primary antibody from Abcam, which was used in this study. The band was aligned with two proteins ladder (Thermo Scientific ladder, Cat#26616 and Bio-Rad ladder, Cat# 1610374) and displayed molecular weight differently. (**B**) Same as (A), but detected by a different primary antibody from Proteintech. (**C**) Lamin B1 protein levels and band shapes were examined with whole cell lysates (WCL) or nuclear fractions (Nucleus) from FN-coated 0.2 kPa or 10 kPa gels. (**D**) Statistical analysis of lamin B1 protein levels among the groups from (C). n= 3 biological replicates. Data are presented as the mean ± SD. Tukey's multiple comparisons test. **(E)** Lamin B1 protein levels and band shapes were examined with or without BSA added. Protein samples were whole cell lysates from soft gels or stiff gels coated with FN.

Figure EV3. Bafilomycin A1 treatment on matrix.
(A, B) Western blot analysis of lamin B1 protein in C2C12 seeded onto FN and gelatin-coated PAA matrices for 30min in the presence of degradation inhibitor (Baf A1, 100 μM). n = 3 biological replicates, Data are presented as the mean ± SD. Two-tailed Student's *t*-test.

Figure EV4. Validation of the specificity of the interaction between Lamin B1 and midnolin.
(A) The ubiquitination level of lamin B1 in C2C12 with MG132. Cells were pre-treated with MG132 for 6 hours and seeded on FN and gelatin-coated PAA matrices for 0.5 hours, the cells were then harvested with IP lysis buffer. IP assay was performed with anti-ubiquitin. **(B)** qRT-PCR to detect the expression of *Midn* transduced with si-*Midn*. n = 3 biological replicates. Data are presented as the mean ± SD. Two-tailed Student's *t*-test was used for statistical analysis. $p = 3.04\times10^{-6}$. **(C, D)** Western blot analysis of lamin B1 proteins in HEK293T cells seeded onto FN-coated PAA matrices after 0.5 hours. n = 3 biological replicates. **(E, F)** Quantification data of lamin B1 intensity and corresponding representative images from negative control scramble siRNA (si-NC) and Lamin B1 knockdown (si-*LMNB1*) HEK293T cells with MG132 treatment on FN-coated PAA matrices for 3 hours. Scale bars, 10 μm. (Tukey's multiple comparisons test. Data were presented as the mean ± SD. >50 cells for each condition). In **(**E**)**, *p* -values are 0.5919, 2×10^{-10}, and 0.4861, respectively. **(G)** Representative images of PLA to detect the interaction between lamin B1 and GFP-midnolin in HEK293T cells with si-NC or si-LMNB1 on FN-coated PAA matrices for 3 hours with MG132 treatment. Scale bar: 10 μm. **(H)** Quantification of PLA signals from experiments as in (G) (Tukey's multiple comparisons test. Data were presented as the mean ± SD. >50 cells for each condition). In **(**E**)**, *p* -values are 1×10^{-10}, 1×10^{-10}, and 0.9125, respectively. **(I, J)** Representative SIM images of midnolin (green) and lamin B1 (red) in C2C12 cells on FN and gelatin-coated PAA matrices with DMSO or MG132 treatment for 0.5 hours. The yellow dots are the colocalization of midnolin and lamin B1 (white arrows). Scale bars, 2 μm. Pearson's correlation coefficient was calculated for lamin B1 and midnolin based on the imaging results in (J). n > 5 cells for each condition. In **(**I**)**, *p* -values are 0.7619, 9.26×10^{-8}, and 0.8161, respectively. **(K)** Schematics of lamin B1 Ig-like domain and CAAX motif truncation. **(L)** HEK293T cells were transfected with Lamin B1 Ig-like domain or CAAX motif truncation and cultured on FN-coated 0.2 kPa gels for 3 hours. **(M)** Normalized midnolin / lamin B1 intensity in (J). n = 3 biological replicates. Data (B, D, I and M) are the mean ± SD, with Two-tailed Student's *t*-test.

Figure EV5. Myoblast differentiation requires moderate lamin B1 protein levels.
(A) qPCR to examine the expression of *Lmnb1* during 24 hours differentiation with scramble siRNA (si-NC) and si-*Lmnb1*. n = 3 biological replicates. Data are presented as the mean ± SD. **(B)** Representative images of WT and *Lmnb1* overexpression C2C12 cells on petri-dishes with 2% horse serum induced differentiation for 3 days. scale bar, 50 μm. **(C, D)** Western blot analysis of lamin B1 protein and Myosin-4 protein in C2C12 during 2% horse serum induced differentiation and corresponding intensity quantification data. n = 3 biological replicates. Data are presented as the mean ± SD.

Figure 1

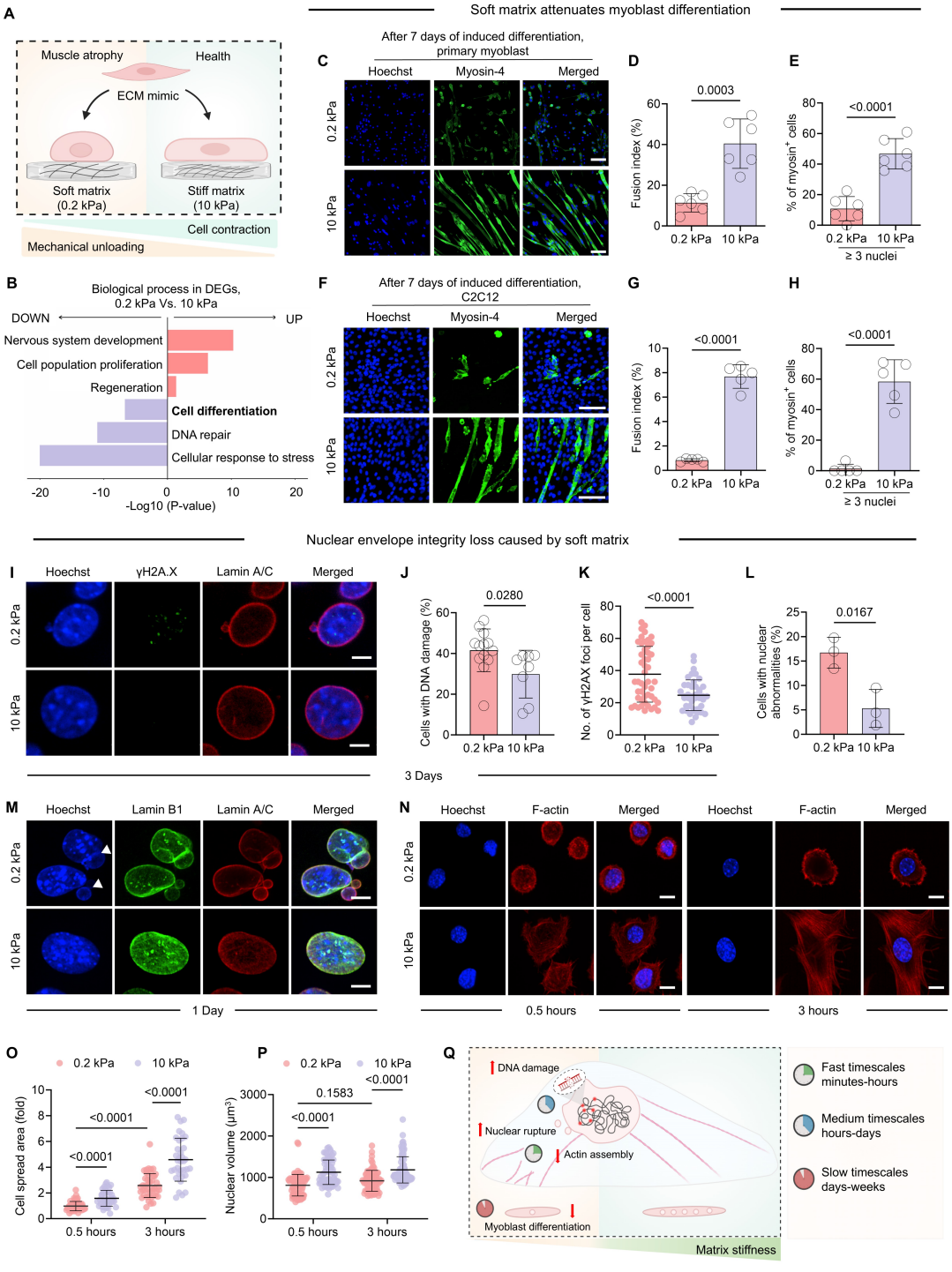

Figure 2

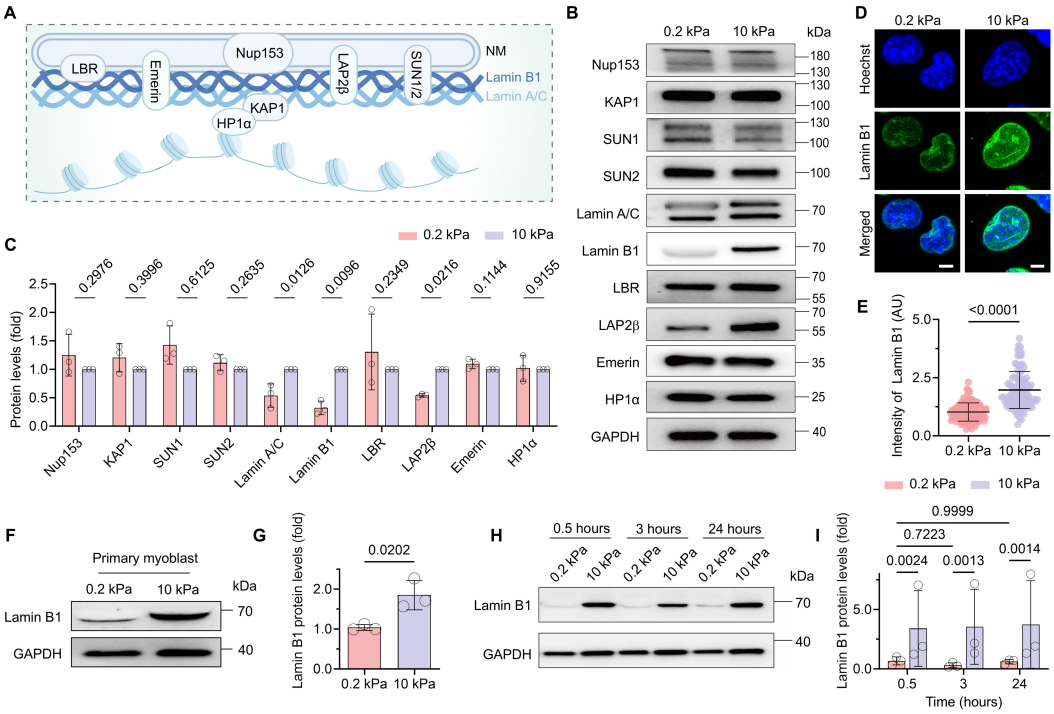

Figure 3

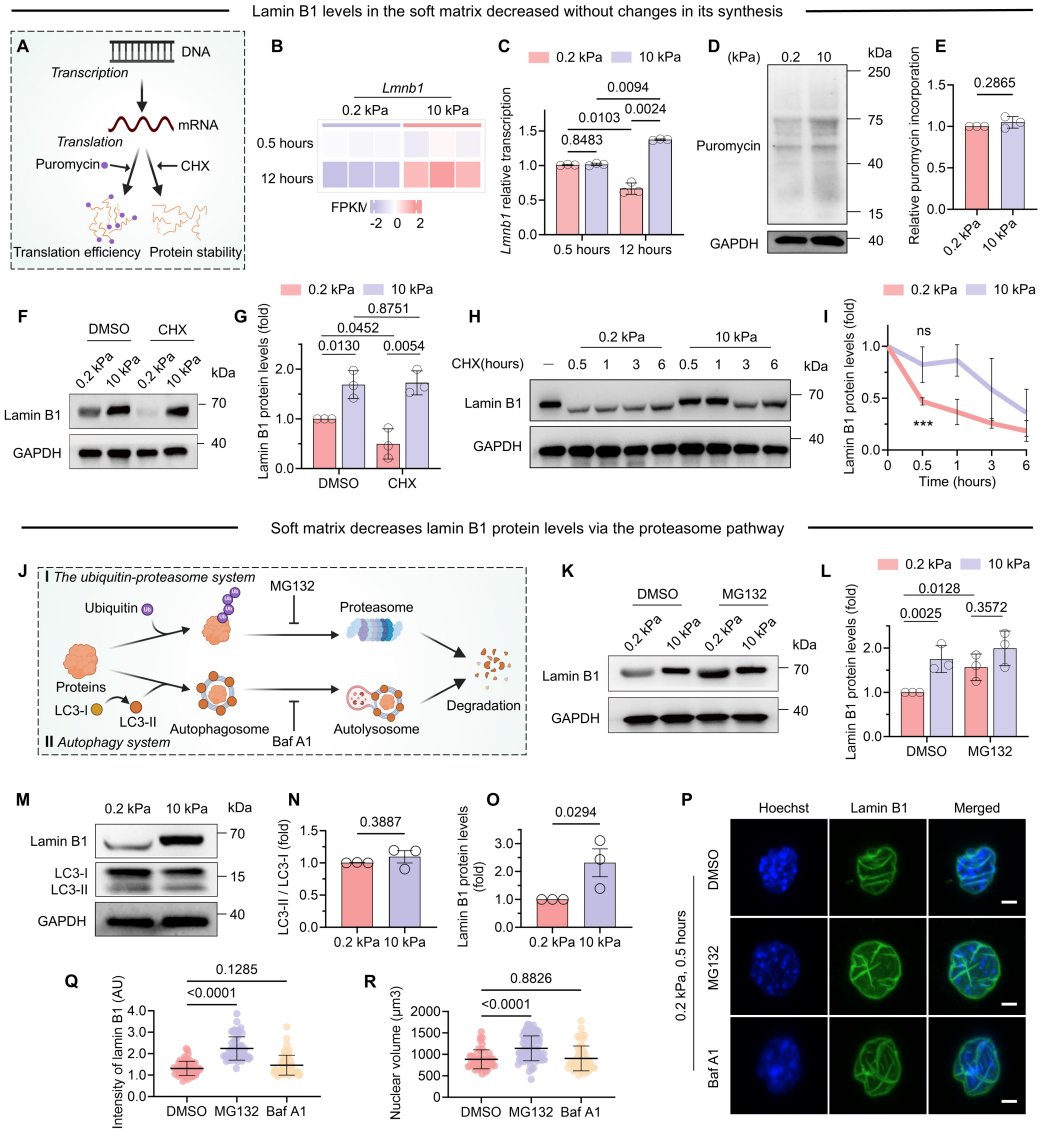

Figure 4

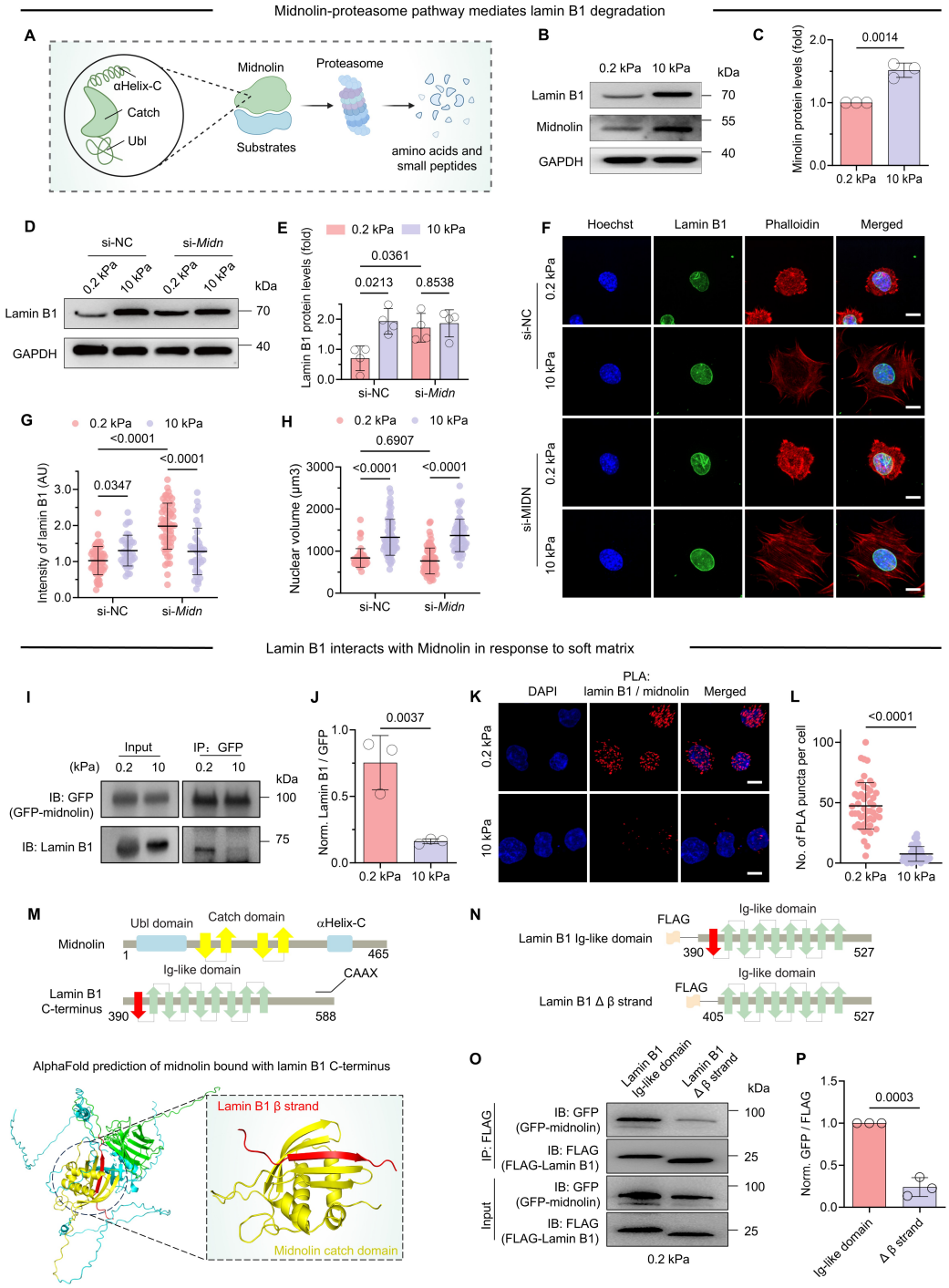

Figure 5

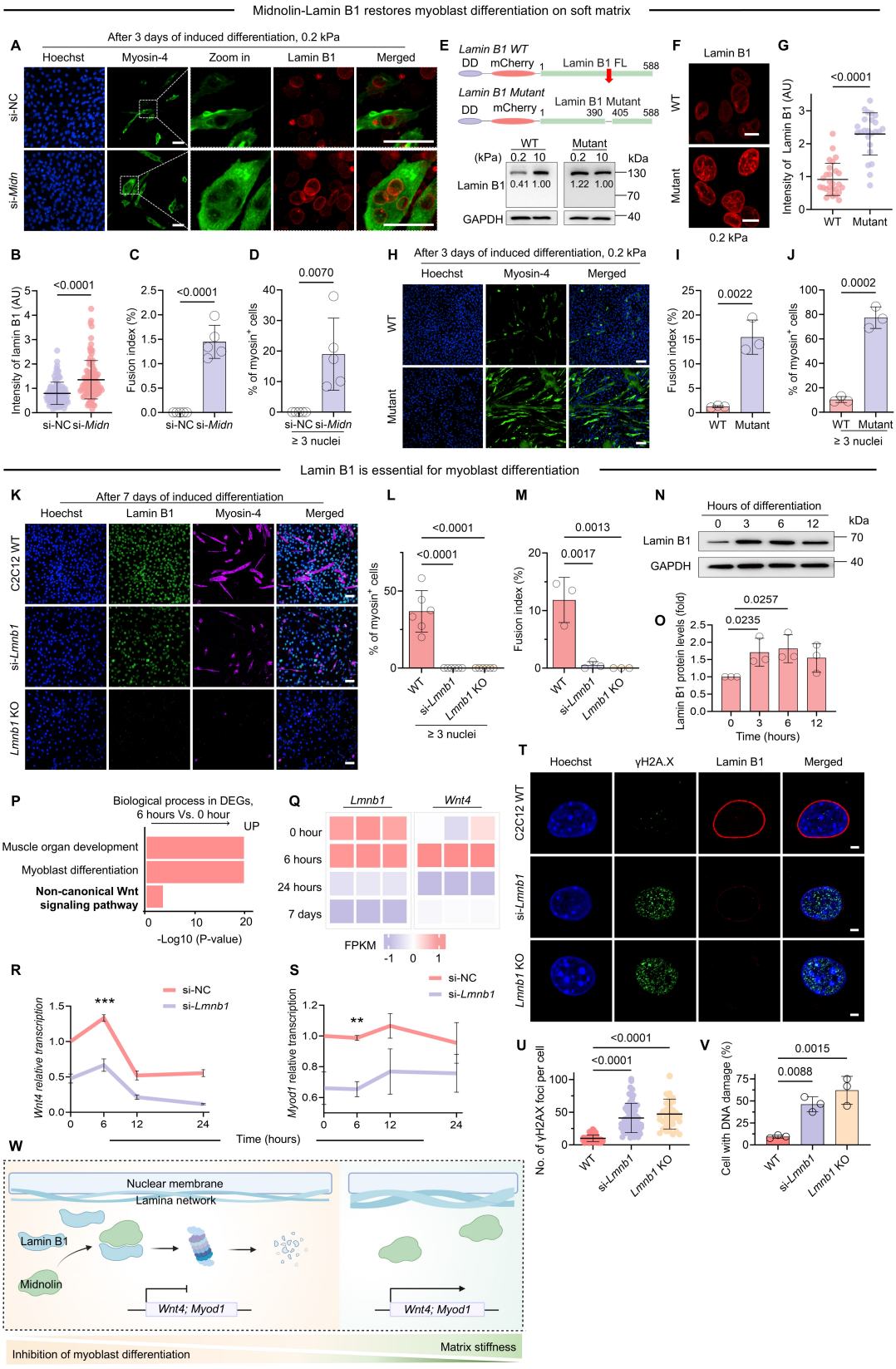

1 **Figure EV1**

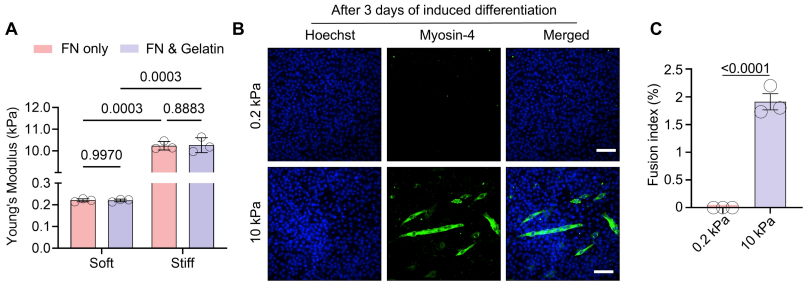

2

3

Figure EV2

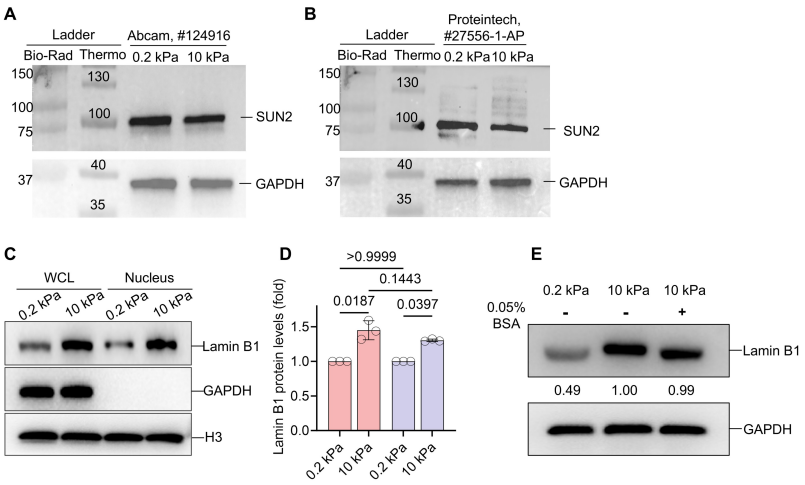

Figure EV3

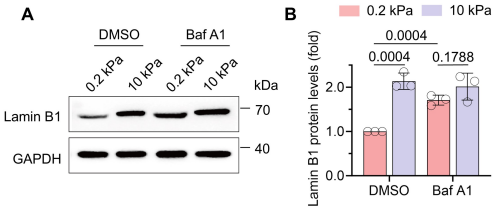

Figure EV4

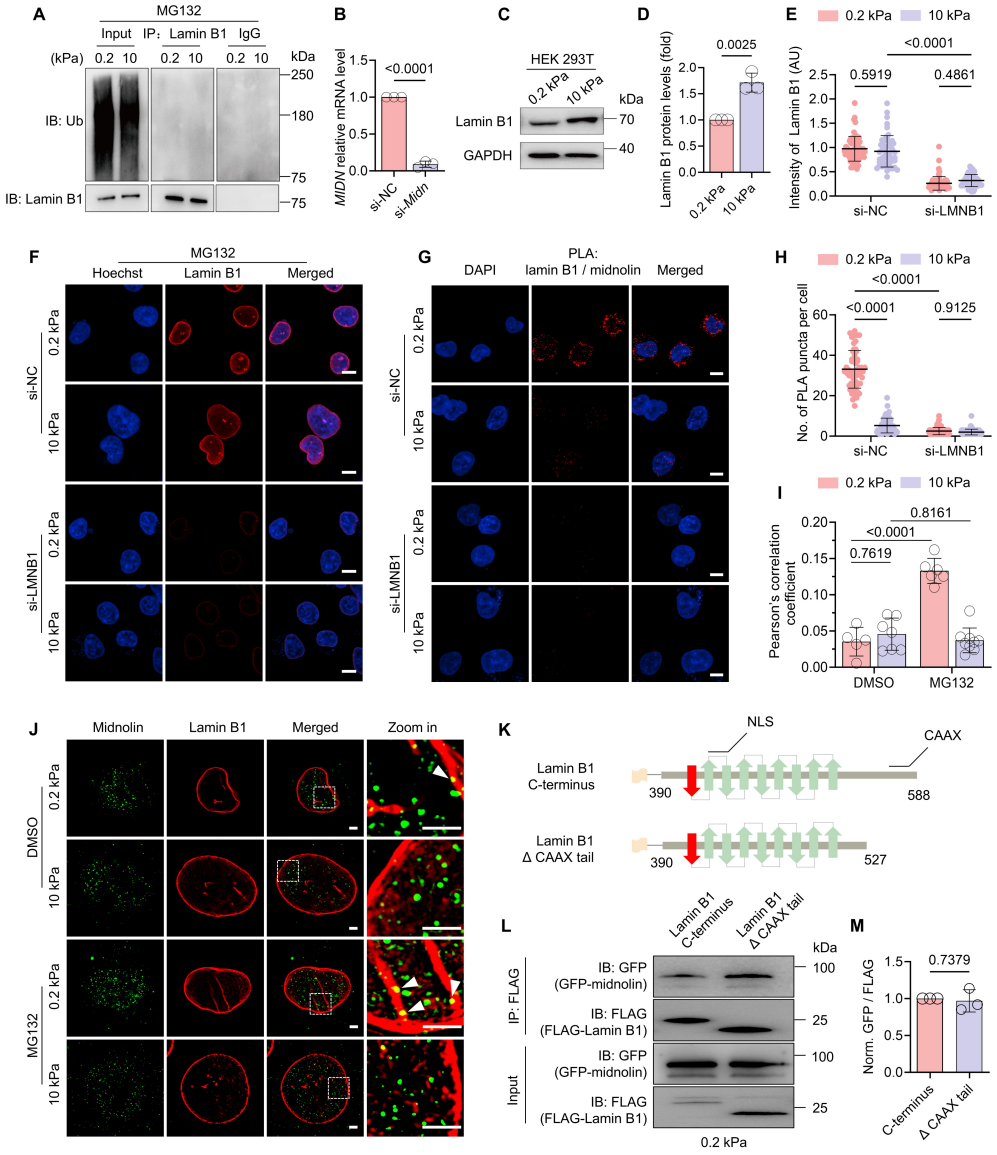

Figure EV5